phys. stat. sol. (a) **116**, 123 (1989)

Subject classification: 61.16; 61.70

Institut für Festkörperphysik und Elektronenmikroskopie der Akademie der Wissenschaften der DDR, Halle (Saale)[1])

Computer Simulation of Diffraction Contrast Images and Lattice Fringe Patterns of Small Spherical Inclusions

By

K. SCHEERSCHMIDT, R. HILLEBRAND, and J. HEYDENREICH

Dedicated to Professor Dr. HEINZ BETHGE on the occasion of his 70th birthday, also on behalf of Prof. V. Schmidt

Diffraction contrast and lattice fringe images of small spherical inclusions in isotropic media are investigated by computer simulation combining the diffraction contrast calculation with the Fourier formalism for considering the electron-optical imaging process including aberrations. Simulated images are presented applying this method to investigate systematically the bright- and dark-fields as well as lattice fringe patterns of the inclusions where the transition region between black and white contrast lobes being of special interest with respect to the inner structure of the defects. In particular, the relations between the black–white diffraction contrast oscillations and the lattice fringe distortions (including shifting, bending, and termination) are studied in connection with the variations in the contrast of precipitates with the thickness of the foil, the depth of the defect in the foil, the deviation from the Bragg reflection condition, and the influence of image aberrations.

Beugungskontrast- und Netzebenenabbildungen von kleinen kugelförmigen Einschlüssen in isotroper Matrix werden mit der Methode der Computersimulation untersucht, wobei Beugungskontrastberechnungen mit dem Fourierformalismus kombiniert werden, um den elektronenoptischen Abbildungsprozeß unter Einbeziehung von Aberrationen zu erfassen. Simulierte Abbildungen werden diskutiert, um systematisch Hell- und Dunkelfeld sowie Netzebenenabbildungen der Einschlüsse zu untersuchen, insbesondere im Gebiet zwischen den Schwarz–Weiß-Kontrastausläufern in Abhängigkeit von der inneren Struktur der Defekte. Der Zusammenhang zwischen den Schwarz–Weiß-Kontrastoszillationen und den Störungen der Netzebenenstreifen (einschließlich Verschiebung, Verbiegung und Abbruch) wird genauer untersucht, wobei die Kontraständerungen an Ausscheidungen als Funktion der Probendicke, der Defekt-Tiefenlage, der Abweichung von den Braggschen Anregungsbedingungen und des Einflusses der Bildaberrationen diskutiert werden.

1. Introduction

In a previous paper [1] a method was described combining the calculation of diffraction contrast amplitudes with the Fourier transformation formalism for simulating bright- or dark-field diffraction contrasts and lattice fringe images of arbitrarily small crystal defects. In a second paper [2] the method of [1] was applied to simulate bright- and dark-field images as well as lattice fringe patterns of a small, inclined, hexagonally shaped, prismatic dislocation loop to derive general rules of the behaviour of lattice fringe contrast with respect to the defect nature and the imaging parameters. In the present paper the method of [1] is applied analogously to [2] to simulate the contrast of small spherical inclusions within isotropic media. As in [2, 3] the outward or inward bendings of fringes caused by the defects do no longer unequivocally prove the precipitate to be of interstitial or of vacancy type. Nevertheless, comprehensive analyses of the fringe distortions (shifting, bending, and termination) with respect to the be-

[1]) Weinberg 2, DDR-4010 Halle (Saale), GDR.

haviour of the black–white contrast oscillations in bright- and dark-field diffraction contrast should yield information on the local defect structure.

For sufficiently small dislocation loops, small defect clusters, and precipitates the black–white (BW) contrast method has been shown to be useful for the defect identification (analysis of BW oscillations, cf. e.g. [2 to 6], the review [7], and the computer-simulated catalogues [8]). The shape of the BW contrast is mainly determined by the long-range part of the elastic distortion field, i.e. it solely depends on the effective strain field of the defect and on the elastic properties of the surrounding matrix.

The BW contrast method fails for very small defects or if the specimen is so thin that anomalous absorption is negligible. Appropriate extreme defocusing (some μm) of the objective lens, however, allows one to transfer the phase information into interpretable black–white contrasts [9, 10]. In this way the BW analysis is extended to cases of vanishing diffraction contrast taking into account the modified oscillation behaviour.

The general features of the BW contrast can be analysed in a first approximation applying the very simplified displacement field of a compression or dilation centre, i.e. a point defect that is an infinitesimally small inclusion having a strength determined by the radius and misfit of the spherical, isotropic particle to be represented within the elastically isotropic medium. The image of such an inclusion shows black and white (BW) contrast lobes separated by a line of no contrast (LNC) and it is characterized by the BW vector $\boldsymbol{l}$ pointing from the black lobe to the white one, which is perpendicular to the LNC and parallel or antiparallel to the diffraction vector $\boldsymbol{g}$ excited. Oscillations of the BW contrast occur due to the variation of the foil thickness, of the depth of the defect, and of the deviation from the exact Bragg excitation. These fundamental contrast properties are only slightly influenced by the shape of the inclusion as well as by the anisotropy of the matrix, whereas the contrast figures are strongly modified with asymmetries of the BW lobes occurring. Thus, for instance, the line of no contrast is straight and perpendicular to the reflection vector $\boldsymbol{g}$ only if the reflecting plane is a symmetry plane of the defect.

Using expensive contrast calculations one can decide whether a certain contrast feature results either from a particular defect property or from the elastic anisotropy — see, e.g., the calculations for the particle as purely hydrostatic stress-free strain [4], for cuboidal shapes [11], and the contrast simulations for different shapes and elastic anisotropy [12 to 14]. For inclusions lying near a surface or having extensions comparable with those of the foil thickness the surface relaxation effects have to be considered additionally [5, 15]. Furthermore, the distortion field inside an inclusion modified, e.g. by incoherent boundaries, inhomogeneous, or otherwise varying eigenstrains, mainly determines the central region of the particle contrast, i.e. the transition region between the black- and white-contrast lobes; here the associated characteristic contrast features are called fine details. These patterns are strongly influenced by even weak image aberrations (defocus of some 10 nm) where the long-range BW behaviour does not change. To avoid misinterpretations of the fine details all the image aberrations have entirely to be taken into consideration. Furthermore, in such calculations for the approximation using the compression or dilation centre the Eshelby model [16] has to be substituted describing the inclusion as a misfitting particle generated by a stress-free effective inelastic strain (see [17] for a general survey of the elasticity of inclusions).

The aim of the present paper, however, is to show the relation between these fine details in diffraction contrast images and the contrast features obtained from lattice fringe imaging, because the fringe distortions are mainly determined by the central defect region. Therefore, the isotropic, spherical particle is considered to additionally include inhomogeneous effective inelastic eigenstrains. A comprehensive systematic

analysis of the contrast oscillation behaviour due to variations in thickness and depth is the basis of investigating and separating the BW behaviour from the fine detail contrast to yield information on the local defect structure.

2. Construction of the Displacement Field

For calculating the displacement field of a spherical inclusion in isotropic media the purely hydrostatic stress-free eigenstrain, given by Eshelby [16] and applied by Ashby and Brown [4], is extended to particles with eigenstrains given by polynomials of coordinates as evaluated by Mura [17, 18]. The displacement field for the particle with hydrostatic stress-free eigenstrain reads

$$\boldsymbol{u}(\boldsymbol{r}) = \begin{cases} \varepsilon \boldsymbol{r}(R_0/r)^3 & \text{for } r \geqq R_0 \,, \\ \varepsilon \boldsymbol{r} & \text{for } r \leqq R_0 \,, \end{cases} \tag{1}$$

where R_0 is the particle radius and $\varepsilon = \delta(1+\nu)/3(1-\nu)$ with the hydrostatic pressure δ and the Poisson constant ν. For coherent particles, having the material elastic constants of the matrix, δ directly describes the volume misfit; thus $\delta > 0$ holds for interstitial or dilation-type inclusions and $\delta < 0$ for vacancy or compression-type defects.

Following Moschovidis and Mura [17, 18] and using the Green's function for isotropic material the displacements for interior and exterior points of an inhomogeneous inclusion Ω can be expressed by

$$\boldsymbol{u}(\boldsymbol{r}) = -(4\pi)^{-1}\, \boldsymbol{grad}\, \Phi_1(\boldsymbol{r}) \,. \tag{2}$$

Here the harmonic and biharmonic potentials are reduced to

$$\Phi_1(\boldsymbol{r}) = \varepsilon \int_{\Omega} \frac{\mu(\boldsymbol{r}')\, \mathrm{d}V'}{|\boldsymbol{r} - \boldsymbol{r}'|} \tag{3}$$

and

$$\Phi_2(\boldsymbol{r}) = \varepsilon \int_{\Omega} \mu(\boldsymbol{r}')\, |\boldsymbol{r} - \boldsymbol{r}'|\, \mathrm{d}V' \,, \tag{4}$$

respectively, for hydrostatic but nonuniform eigenstrains

$$\varepsilon^*_{ij}(\boldsymbol{r}) = \varepsilon \mu(r)\, \delta_{ij} \,, \tag{5}$$

with the "body density" $\mu(r)$.

The properties of the potentials $\Delta\Phi_2 = 2\Phi_1$ and

$$\Delta\Delta\Phi_2 = 2\Delta\Phi_1 = \begin{cases} -8\pi\mu(r) & \text{for } r \text{ in } \Omega \,, \\ 0 & \text{for } r \text{ out of } \Omega \end{cases} \tag{6}$$

are not changed and guarantee that the displacements fulfil the basic equations of elasticity and the compatibility conditions ($\Delta = \boldsymbol{div}\, \boldsymbol{grad}$).

With the elementary solution for a sphere Ω of radius R_0,

$$\Phi_1(\boldsymbol{r}) = 4\pi\varepsilon \int_0^{R_0} \mu(R)\, \mathrm{Min}\,(R^2/r,\, R)\, \mathrm{d}R \,, \tag{7}$$

and the additional condition for the body density,

$$\int_0^{R_0} \mu(R)\, R^2\, \mathrm{d}R = R_0^3/3 \,, \tag{8}$$

the displacement field of the inhomogeneous sphere is reduced in the far-field to those of the Ashby-Brown precipitate (1) and may read

$$\boldsymbol{u}(\boldsymbol{r}) = \begin{cases} \varepsilon \boldsymbol{r} (R_0/r)^3 & \text{for } r \geqq R_0 \,, \\ \varepsilon \boldsymbol{r}/r^3 \int_0^r \mu(R)\; R^2 \,\mathrm{d}R & \text{for } r \leqq R_0 \,. \end{cases} \tag{9}$$

Because of the singularity at $\boldsymbol{r} = \boldsymbol{r}'$ the integrals do not exist in the sense of Riemann integrals, but this difficulty can be avoided using only polynomials for the body density with exponents greater than -2 at r and including logarithmic terms. The term r^{-3} must be interpreted as a distribution-type function, which allows one to replace the transition from inhomogeneity to the Ashby-Brown precipitate for R_c different from R_0.

Hence,

$$\boldsymbol{u}(\boldsymbol{r}) = \begin{cases} \varepsilon \boldsymbol{r} (R_0/r)^3 & \text{for } r \geqq R_c \,, \\ \varepsilon \boldsymbol{r} [a \ln (r/R_0) + \sum_{j \geqq -3} b_j (r/R_0)^j] & \text{for } r \leqq R_c \,. \end{cases} \tag{10}$$

Fulfilling the additional condition (8) denotes continuity of $\boldsymbol{u}(\boldsymbol{r})$ at $r = R_c$ and demands

$$(R_0/R_c)^3 = a \ln (R_c/R_0) + \sum_{j \geqq -3} b_j (R_c/R_0)^j \,, \tag{11}$$

which is reduced to

$$\sum_{j \geqq -3} b_j = 1 \quad \text{for} \quad R_c = R_0 \,.$$

For $R_c \approx 0$ the displacements (10) are those of pure dilation or compression centres, which in (10) are also included for $a = 0$, $b_{-3} = 1$ fulfilling condition (11). If condition (11) is not maintained, the additional jump of $\boldsymbol{u}(\boldsymbol{r})$ at $r = R_c$ can be interpreted as a sliding inclusion or incoherent precipitate.

3. Method of Computer Simulation

The computer simulation of defocus diffraction contrast as well as of lattice fringe images of crystal defects has been carried out by the method described in the previous paper [1], combining the calculation of diffraction contrast amplitudes with the Fourier transformation formalism.

The diffraction contrast amplitudes are calculated by solving the Howie-Whelan equations using Runge-Kutta integration procedures or Thoelen's matrix multiplication method. To minimize the numerical effort an amplitude interpolation procedure is applied in such a manner that only about 20% of the pixels are integrated directly. The imaging process is described by Fourier analysis and Fourier synthesis of the amplitudes related to the image pixels, considering here the electron microscope aberrations on the basis of the contrast transfer function.

For comparison, HREM micrographs were calculated using a modified multislice program [19, 20] with discrete Fourier transform and convolution (128 × 128 pixels). Without discrete real-space sampling the Fourier transform of the projected potential of each slice is directly evaluated from the atomic coordinates of the structure model and the associated atomic scattering amplitudes. For a sufficient accuracy in applying the method to crystals containing lattice defects with a nonvanishing elastic far-field the lateral extension of supercells must be dimensioned to avoid effects of aliasing and truncation.

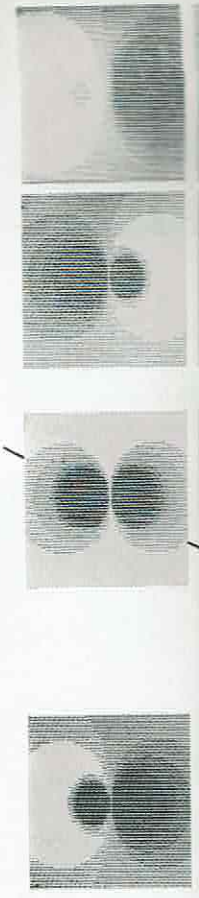

Fig. 1. Calculated
ness t/ξ_g and the d
$\boldsymbol{g} = (1\bar{1}1)$, $\boldsymbol{e} = (1$
t_0/ξ_g (vertical)

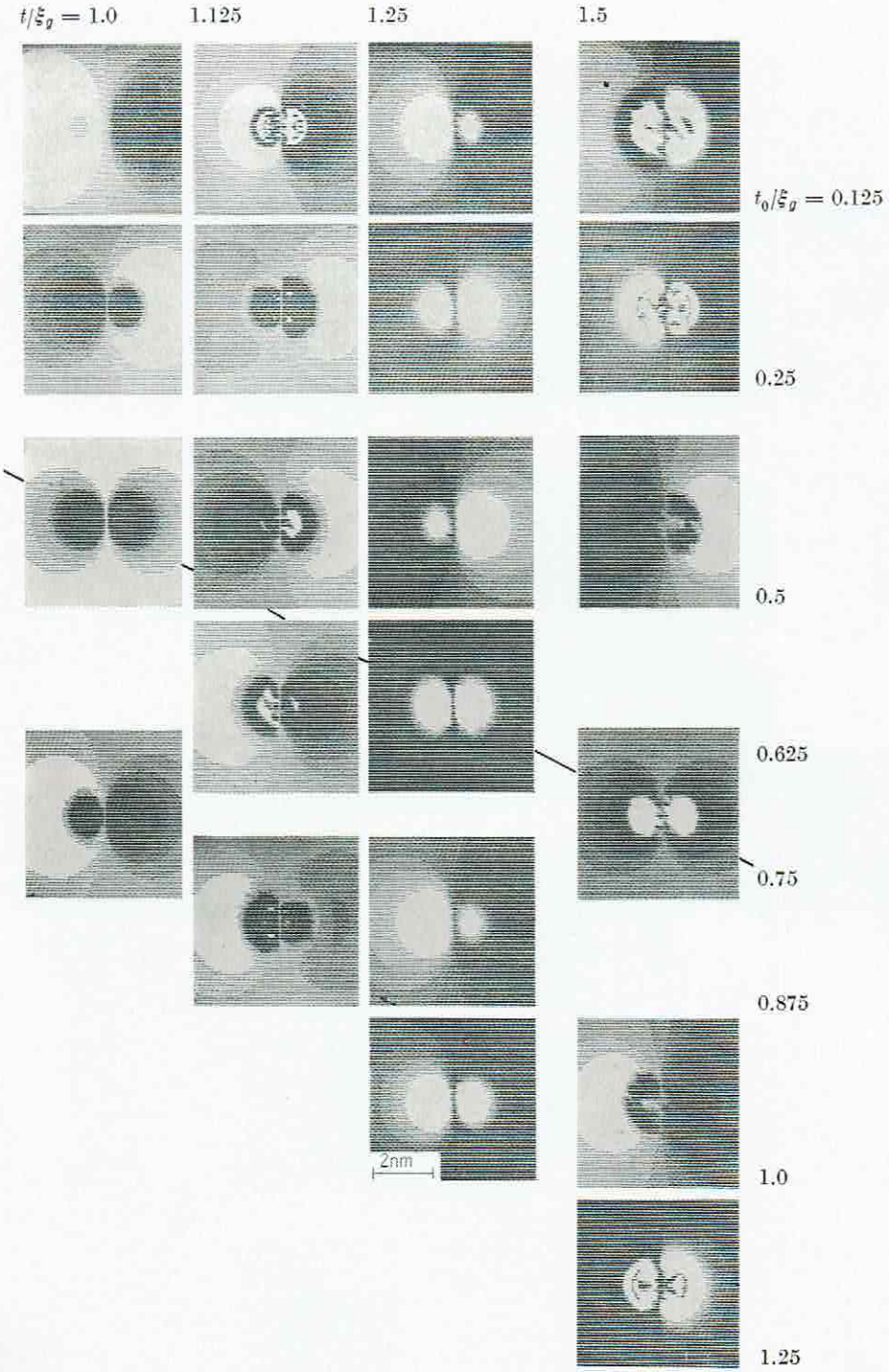

Fig. 1. Calculated bright-field images I_{000} of a dilation centre as a function of the foil thickness t/ξ_g and the depth position t_0/ξ_g of the defect centre. Parameters: $\bar{\varepsilon} = g\varepsilon\xi_g = 2$, $R_0 = 0.05\xi_g$, $\boldsymbol{g} = (1\bar{1}1)$, $\boldsymbol{e} = (110)$, $\boldsymbol{w}_{1\bar{1}1} = 0$, $C_s = \Delta = 0$, foil thickness t/ξ_g (horizontal), depth of defect t_0/ξ_g (vertical)

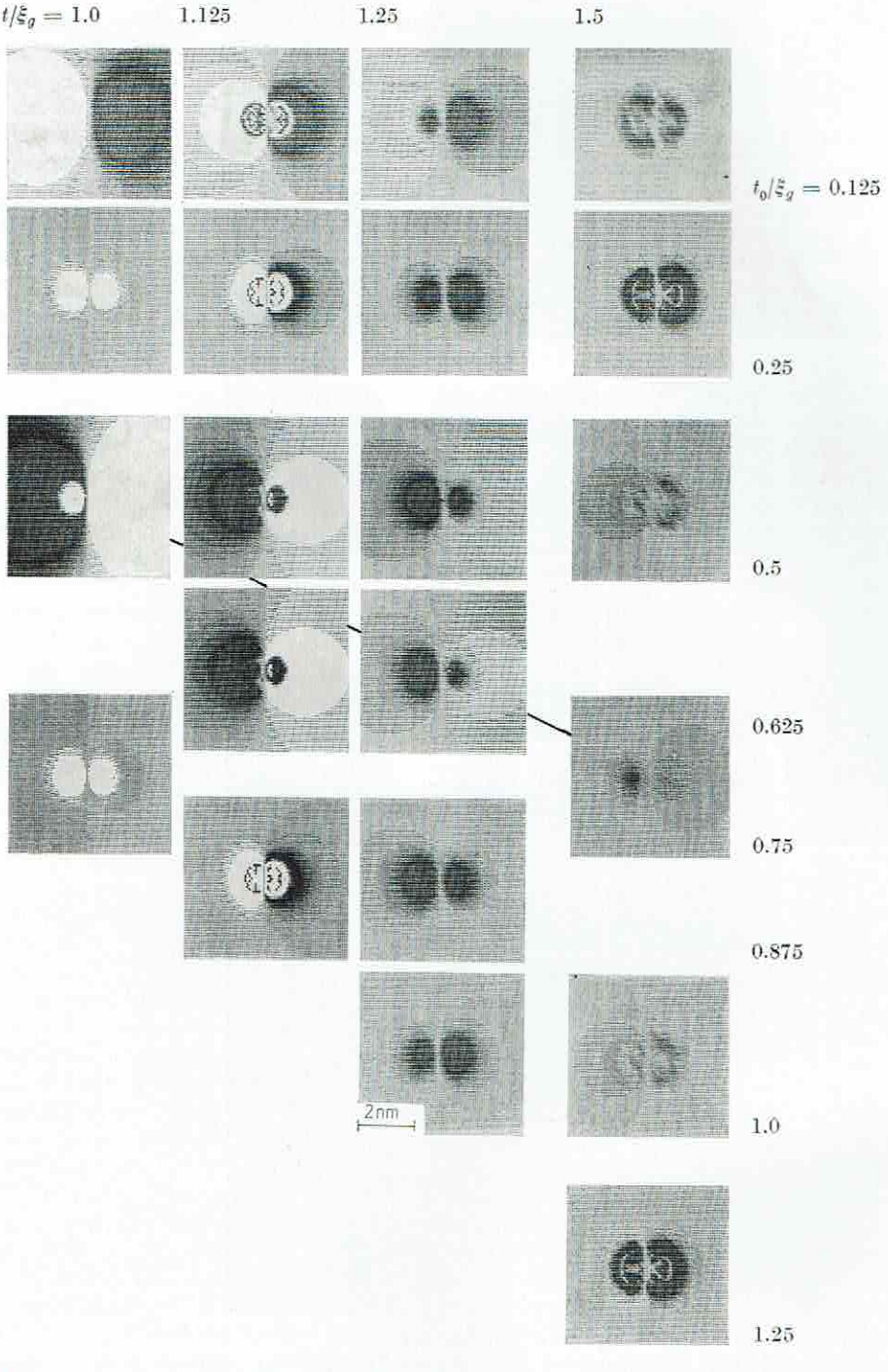

Fig. 2. Calculated dark-field images $I_{1\bar{1}1}$ of a dilation centre as a function of the foil thickness t/ξ_g and the depth position t_0/ξ_g of the defect centre (parameters: see Fig. 1)

Computer Simulatio

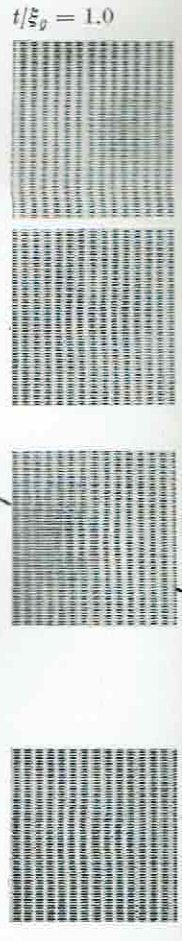

Fig. 3. Calculated
thickness t/ξ_g and t

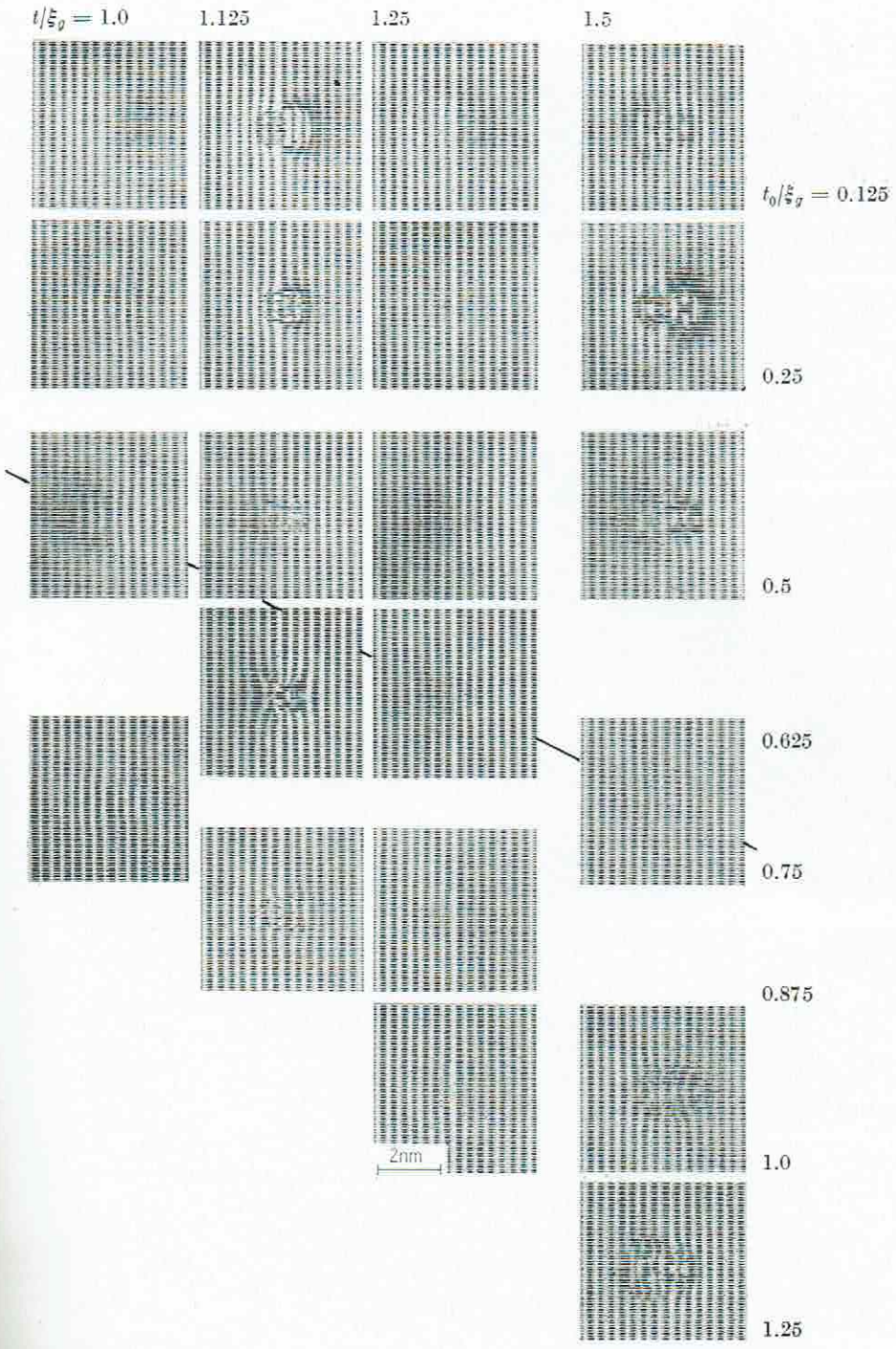

Fig. 3. Calculated (111)-lattice fringe contrast of a dilation centre as a function of the foil thickness t/ξ_g and the depth position of the defect centre t_0/ξ_g (parameters: see Fig. 1)

Fig. 4. Tilt series (deviation w) of bright-field BF, dark-field DF and lattice fringe LF images for a spherical precipitate. $\boldsymbol{g} = (111)$, $\boldsymbol{e} = (110)$, $\varepsilon = 2$, $t = 1.125\xi_g$, $t_0 = 0.125\xi_g$, $R_0 = 0.625\xi_g$; $C_s = \Delta = 0$

Fig. 5. Through-focus series (Δ) of BF and LF contrast of a spherical precipitate for different depth t_0 and foil thickness t. $\boldsymbol{g} = (111)$, $\boldsymbol{e} = (110)$, $\bar{\varepsilon} = 2$, $R_0 = 0.05\xi_g$; $U = 100$ kV, $C_s = 1.4$ mm, $\alpha = 4$ nm^{-1}

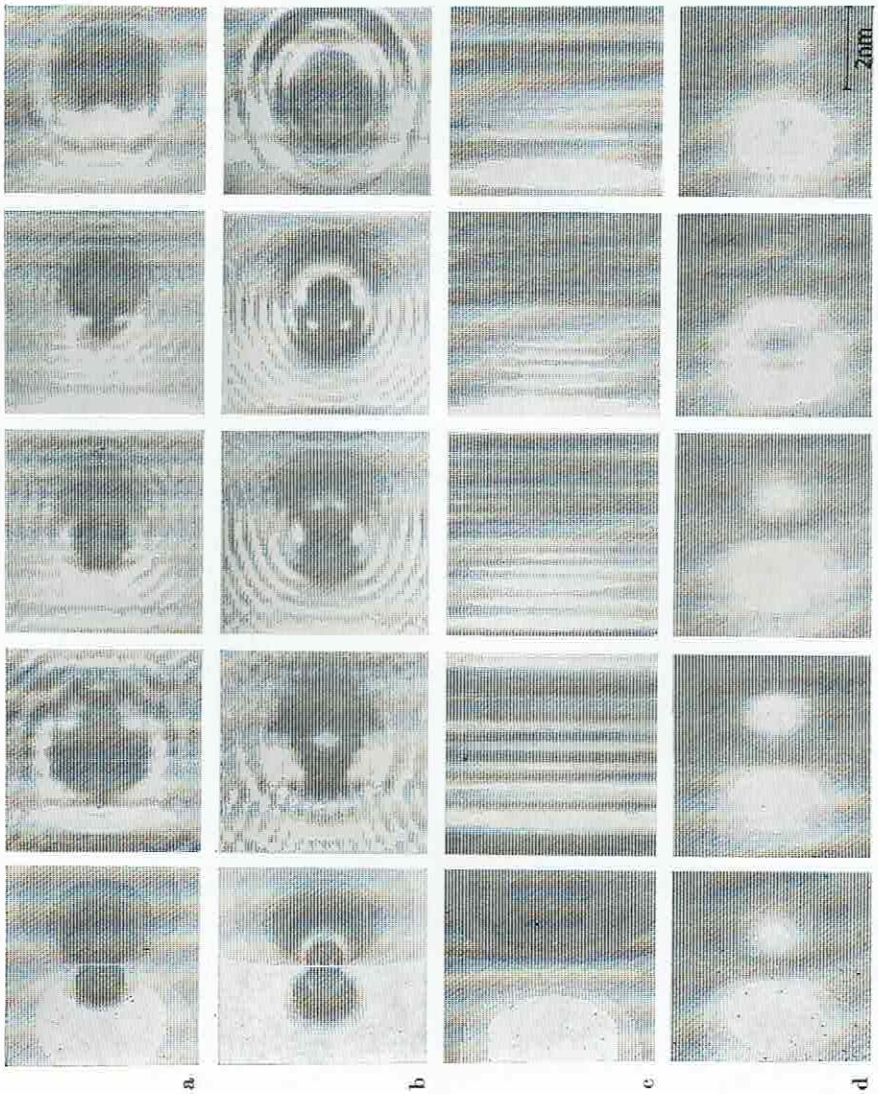

Fig. 6. Defocused (Δ) bright-field contrast of a spherical precipitate for different thickness t, depth t_0 and excitation partmeter w. Parameters: $\boldsymbol{e} = (110)$, $\boldsymbol{g} = (111)$, $\varepsilon = 20$, $R_0 = 0.05\xi_g$, $U = 100$ kV, $C_s = 1.4$ mm, $\alpha = 4$ nm^{-1}. a) $t/\xi_g = 0.75$, $t_0/\xi_g = 0.125$, $w = 0$; b) $t/\xi_g = 0.75$, $t_0/\xi_g = 0.5$, $w = 1$; c) $t/\xi_g = 5$, $t_0/\xi_g = 0.125$, $w = 0$; d) $t/\xi_g = 5$, $t_0/\xi_g = 1$, $w = 5$

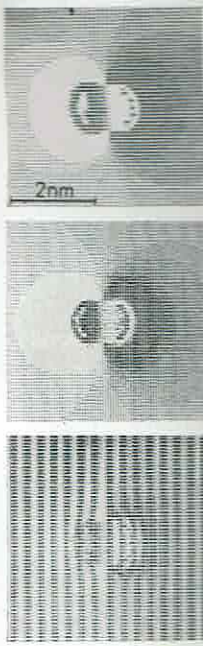

Fig. 7. BF, DF, an
strain centre. Para
$C_s = \Delta = 0$

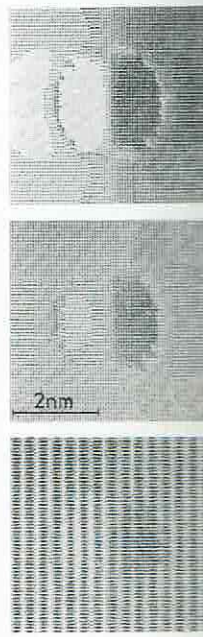

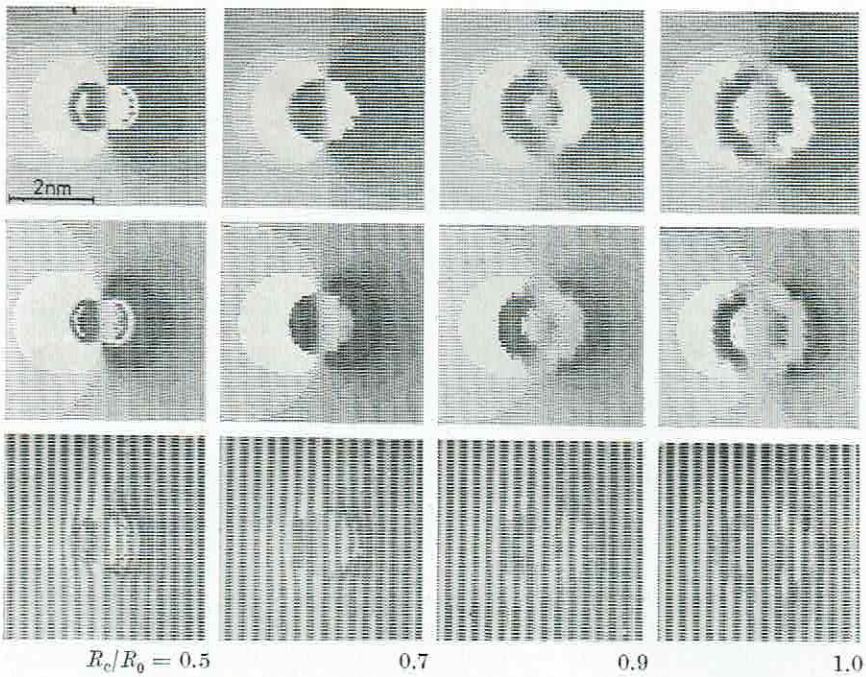

Fig. 7. BF, DF, and LF images of a spherical precipitate for different radii R_c of the homogeneous strain centre. Parameters: $\boldsymbol{g} = (1\bar{1}1)$, $\boldsymbol{e} = (110)$, $t = 1.125\xi_g$, $t_0 = 0.125\xi_g$, $\bar{\varepsilon} = 2$, $R_0 = 0.05\xi_g$; $C_s = \Delta = 0$

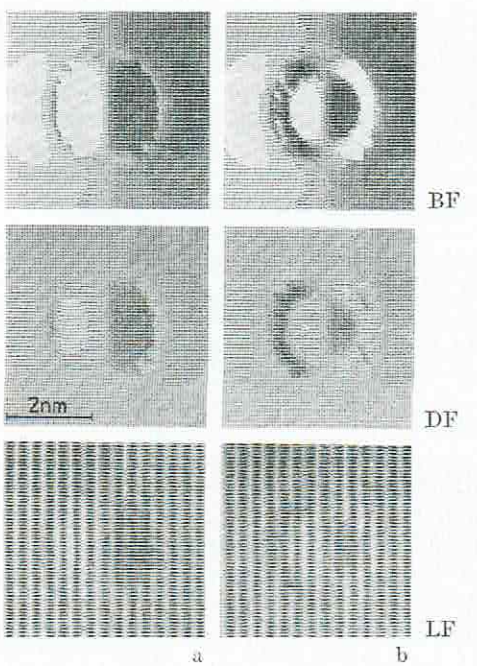

Fig. 8. Bright-field (BF), dark-field (DF), and lattice fringe (LF) images of a spherical inclusion with an inhomogeneous eigenstrain: a) $b_{-3} = 0.1$, $b_{-1} = 5$, $a = 5$, b) $b_{-2} = 0.1$, $b_{-1} = 0.5$, $b_1 = 0.2$, $a = 0$. Parameters: $\boldsymbol{g} = (1\bar{1}1)$, $\boldsymbol{e} = (110)$, $w = 0$, $t = 1.125\xi_g$, $t_0 = 0.125\xi_g$, $\bar{\varepsilon} = 2$, $R_0 = 0.05\xi_g$, $C_s = \Delta = 0$

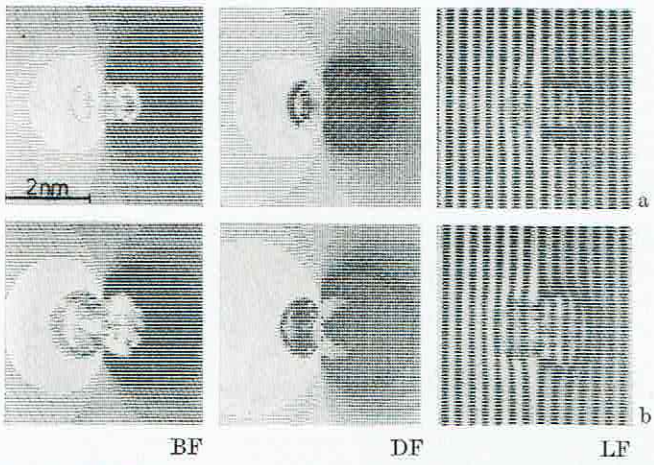

Fig. 9. BF, DF, and LF images of a spherical inclusion near the upper surface with (depth a) $t_0 = 0.07\xi_g$, b) $t_0 = 0.125\xi_g$ for different constrained strain a) $\bar{\varepsilon} = 2$, b) 5. Parameters: $\boldsymbol{g} = (1\bar{1}1)$, $\boldsymbol{e} = (110)$, $w = 0$, $t = 1.125\xi_g$, $R_0 = 0.05\xi_g$, $C_s = \Delta = 0$

The simulation procedures briefly outlined are applied to investigate contrast features caused by small spherical inclusions as characterized in Section 2. In Fig. 1 to 3 the bright-field (BF), dark-field (DF), and lattice-fringe (LF) contrasts are systematically studied. In order to discriminate the specimen signal itself of the final images from the aberrational influence of the electron microscope perfect contrast transfer (in-focus $\Delta = 0$, aberration free $C_s = 0$) is assumed. For an exact Bragg orientation (f.c.c. lattice, [110] incidence, $(1\bar{1}1)$ reflex with $w_{1\bar{1}1} = 0$) the BF, DF, and LF patterns are shown in tables, where foil thickness and depth position t_0 of the defect are the significant specimen parameters.

A selected tilt series is presented in Fig. 4 to investigate the effect of the deviation from the exact Bragg position. Fig. 5 and 6 reveal the influence of the contrast transfer function on the BF as well as on the LF contrast assuming factual aberrations of a 100 kV microscope ($C_s = 1.4$ mm). Based on these systematic analyses Fig. 7 to 9 deal with the connection between contrast details and the assumed inner structure of the inclusions (eigenstrains). Finally, the influence of many-beam situations is studied using three-beam and multislice calculations (Fig. 10 and 11). This enables the comparison of the LF calculations with the multislice calculations of e.g. small, spherical precipitates [21], cuboidal nano-precipitates [22], and Guinier-Preston zones [23]. Analogously to the discussions of the phase influencing behaviour of plate-like precipitates [24] the calculations prove that the phase difference between BF and DF is the contrast determining factor in LF patterns and in many-beam images (HR).

While for the diffraction contrast calculations relative coordinates and parameters are used, which are related to the extinction distance assumed, multislice calculations employ absolute values, which are based on the structure and dimension of the lattice and the atomic scattering amplitudes. To diffraction contrast calculations a beam incidence of $\boldsymbol{e} = [110]$ and an excited reflex of $\boldsymbol{g} = \{111\}$ type are applied, which e.g. for gold means an extinction distance (two-beam value of standard textbooks for 100 kV) of $\xi_g = 18.3$ nm and lattice fringes with $d = 0.236$ nm, whereas for silicon $\xi_g = 60.5$ nm and $d = 0.314$ nm can be assumed. Many-beam calculations yield to $\xi_g = 4$ nm for gold and $\xi_g = 25$ nm for silicon. In the following $\xi_g = 25$ nm is applied, i.e. in interpreting the calculated images by assuming always $R_0 = 0.05\xi_g$ and an

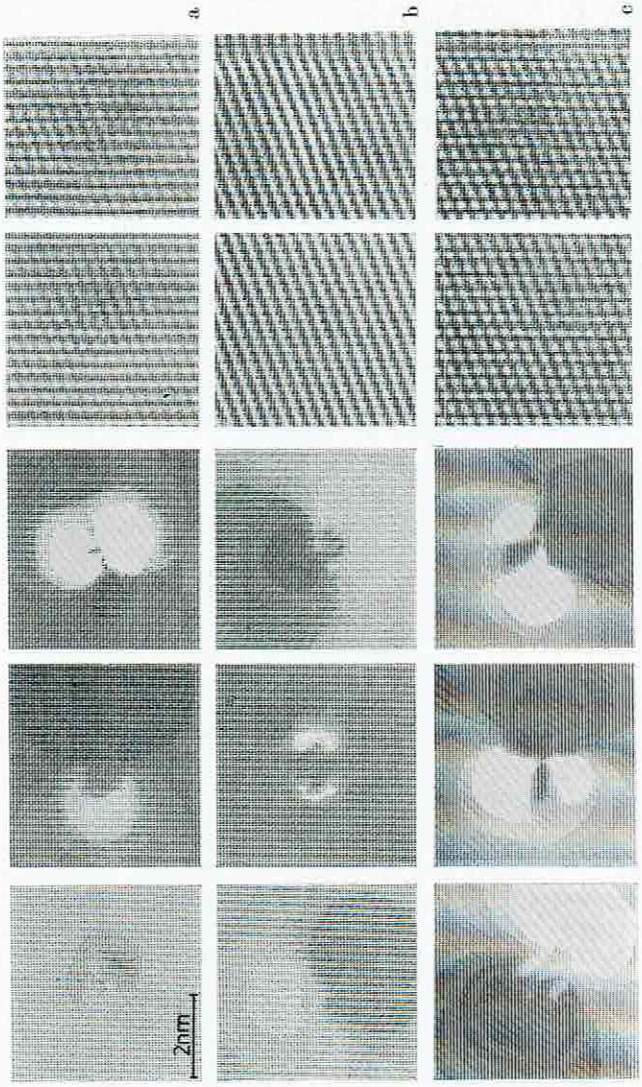

Fig. 10. Three-beam images (HR) for two defocus values ($\Delta = 0$ and 86 nm) with corresponding BF and DF contrast (excitation w). Parameters: $\boldsymbol{e} = (110)$, $\boldsymbol{g}_1 = (1\bar{1}1)$, $\boldsymbol{g}_2 = (11\bar{1})$, $\bar{\varepsilon} = 2$, $t = 1.125\xi_g$, $t_0 = 0.125\xi_g$, $U = 100$ kV, $C_s = 1.4$ mm. a) $w_{111} = 0$, $w_{11\bar{1}} = 5$; b) 5, 1; c) 1, 1

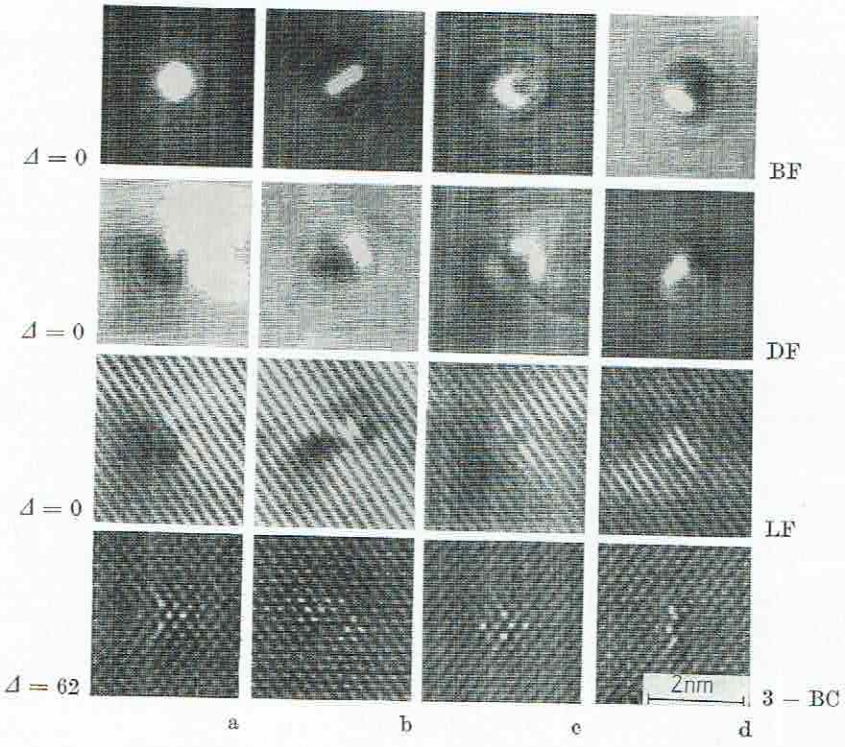

Fig. 11. "Multislice" image calculations of bright-field, dark-field ($\Delta = 0$, $s = 2.1\,\mathrm{nm}^{-1}$), lattice fringe ($\Delta = 0$, $s = 2.5\,\mathrm{nm}^{-1}$), and three-beam (HR) ($\Delta = 62$ nm, $s = 3\,\mathrm{nm}^{-1}$) images of a spherical dilation centre for different beam incidence: tilt of pole $\boldsymbol{p} = (000)$ (a), $1/4(\bar{7}, \bar{7}, \bar{2}0)$ (b), $1/2(11\bar{1})$ (c, d). Parameters: $U = 100$ kV, $C_s = 1$ mm, $\boldsymbol{e} = (110)$, $R_0 = 1.6$ nm, $\varepsilon = 0.05$, $N = 21$ ($t \approx 1.5\xi_g$); $t_0 = t/2$ (a to c), $t/5$ (d)

image size of $0.2\xi_g$ this implies an absolute defect radius of $R_0 = 1.25$ nm as well as an image dimension of 5 nm. The corresponding relative defect strength $\bar{\varepsilon} = g\varepsilon\xi_g = 2$, therefore, describes an absolute misfit of $\varepsilon = 0.025$. The calculations of defocused images and three-beam cases finally require an absolute value of the extinction distance to be fixed for scaling the CTF.

The specimen model for the multislice calculations is established by a variable sequence (sandwich) of perfect and differently distorted crystal slices according to the distance from the defect centre. Fulfilling the numerical requirements a supercell is constructed having an extension of 6×9 Au(110) unit meshes ($3.47 \times 3.68\,\mathrm{nm}^2$) and containing 216 atoms. For the assumed size and strength of the defect ($R_0 = 1.6$ nm, $\varepsilon = 0.05$, dilation centre) the local displacements of the atoms are vanishing near the lateral cell boundaries to fulfil the conditions of periodic continuation. Five different model slices of $\Delta z = 0.288$ in thickness are sufficient to approximate the defect structure parallel to the beam direction. The multislice recursion was carried out including approximately 7000 beams. The microscope imaging conditions (BF, DF, LF, HR) are adjusted by the position and diameter (α_{hkl}) of the aperture in the plane of the diffraction pattern.

4. Diffraction Contrast

Calculated diffraction contrast images of an isotropic dilation centre are shown in Fig. 1 (BF) and 2 (DF). The contrast phenomena may be discussed in terms of a central region and the extended black–white (BW) lobes. The oscillating BW contrast arises due to the strains caused by the defect in the surrounding matrix under dynamical two-beam conditions, because for the defect $g\varepsilon R_0^3/\xi_g^2 < 0.2$ is fulfilled (otherwise black-lobe contrast with LNC occurs [4 to 8]). Furthermore, for $R_0 = 0.05\xi_g$ and $\bar{\varepsilon} = g\varepsilon\xi_g = 2$ applied here, the defect is hardly visible, whereas $\bar{\varepsilon} = 5$ and 20 used in Fig. 9 and 6, respectively, give a better contrast (10% visibility criterion for small radii $g\varepsilon R_0^2/\xi_g > 0.01$ [4 to 8]). The Ashby-Brown rule $\varepsilon(\boldsymbol{g} \cdot \boldsymbol{l}) < 0$ [4] is fulfilled which for defects of interstitial type ($\varepsilon > 0$) in the upper surface layer L_0 ($t < \xi_g/4$) determines the BW vector $\boldsymbol{l}$ to be antiparallel to the diffraction vector $\boldsymbol{g}$.

The sign of $\boldsymbol{g} \cdot \boldsymbol{l}$ alternates according to the depth t_0 of the defect with a $\xi_g/2$ periodicity except in the surface layer $\xi_g/4$, which is determined by relaxation effects (cf. Fig. 9). The vector $\boldsymbol{g}$, however, is always perpendicular to $\boldsymbol{l}$ independent of t_0 and t. Excluding the region close to the surface ($t_0 < \xi_g/4$, $t - t_0 < \xi_g/4$) the existing depth periodicity can be characterized by the depth layers L_n of alternating BW vectors,

$$\xi_g/4 + (n-1)\,\xi_g/2 \leqq t_0 \leqq \xi_g/4 + \eta\xi_g/2 \tag{12}$$

(assuming a perfect contrast transfer) [4 to 8]. At the layer boundaries $(2n+1)\,\xi_g/4$ the BW contrast degenerates to a black-dot contrast with non-unique BW vector $\boldsymbol{l}$. Analogous to the thickness fringes in wedge-shaped crystals the layer periodicity L_n is overlaid with a periodicity of the diffraction contrast with respect to the specimen thickness t; the contrast for BF reaches its maximum at $t = (2m+1)\,\xi_g/2$, and for DF at $t = m\xi_g$.

The intervals considered in Fig. 1 and 2 of the crystal thickness $t[1\xi_g, 1.5\xi_g]$ (horizontal) and of the depth of the defect $t_0\,[0, t]$ (vertical), are thus representative of all contrast features observable due to the periodicity of the BF and DF in diffraction contrast with respect to t and t_0. Accordingly, the specimen thicknesses chosen around $1\xi_g$ are appropriate for experiments as well as for contrast calculations at higher spatial resolution applying the column approximation. The arrangements of calculated images in Fig. 1 and 2 summarize the above BW contrast behaviour in BF and DF imaging. In addition to the periodic behaviour discussed the BF and DF diffraction contrasts in Fig. 1 and 2 clearly show that for inclusions in the upper half of the specimen ($t_0 < t/2$) the black–white vectors of the contrast lobes have the same sign in BF and DF patterns. If the crystal defect lies below the middle of the foil the contrast vectors of BF and DF turn opposite, and the image intensities are almost complementary. In the $(t - t_0)$ table the line $t_0 = t/2$ is marked; for this special depth position of the defect the bright field contrast patterns are symmetrical.

Compared with the background intensity the central contrast regions (in the neighbourhood of the LNC) of associated BF and DF patterns are almost the same. For some parameter combinations, particularly for the thicknesses $t = 1.125\xi_g$ and $t = 1.5\xi_g$, the fine structure and the phase distributions associated are more complex than for $t = 1.0\xi_g$ and $t = 1.25\xi_g$.

5. Lattice Fringes

While lattice fringe patterns of undistorted crystals show only black–white fringes of a sinusoidal intensity profile, crystal defects cause modifications [1]. The fringe structure may essentially be influenced by significantly varying the phase difference be-

tween BF and DF amplitudes over a small area. The resulting fine structure of the lattice fringes sufficiently rich in contrast is detectable if these phase discontinuities arise from comparable intensities in the BF and DF contrasts. The contrast features in the lattice fringe images of the simulated dilation centre (cf. Fig. 1 to 3) illustrate these general considerations.

According to the crystal defect for all LF patterns, presented in Fig. 3, the rotational symmetry of the dilation centre does not provide any additional lattice plane in the surrounding matrix. The residual diffraction contrast of the crystal defect as well as the fringe modifications depend on the depth position t_0 of the defect and on the crystal thickness t. There are three types of lattice contrast features:

(i) Bending of the LF in the central defect region according to the fine structure in BF and DF patterns and mostly accompanied with dark shadows. For the depth interval $t_0 < \xi_g/2$ outward bending occurs whereas inward bending is observed for $t_0 > \xi_g/2$.

(ii) Terminated additional fringes occur within the outward-bent structures, whereas for inward bending the outer fringes continue in a smaller number of inner fringes.

(iii) Displacement (shift) of the fringe system in the central region of the defect with respect to the undisturbed matrix fringes characterizes the mean phase difference between BF and DF amplitudes.

For the thicknesses $t = 1.0\xi_g$ and $t = 1.25\xi_g$ as well as for defects in the middle of the foil, $t_0 \approx \xi_g/2$ the contrast caused by the crystal defect fades. Residual diffraction contrast occurs if the extended BW lobes in BF and DF images have the same sign (BW vector), but the fringe modifications (i) to (iii) are factually determined by the fine details of the diffraction contrast, requiring comparable intensities in the corresponding image positions with respect to the background intensity.

6. Influence of Specimen Tilt

In the tables of Fig. 1 to 3 the exact Bragg orientation was assumed for all contrast investigations with the specimen thickness and defect position varying. To study the influence of specimen tilt in Fig. 4 the bright-field (BF), dark-field (DF), and lattice fringe (LF) contrasts of the dilation centre are displayed for the excitation w of the diffraction vector $\boldsymbol{g} = (1\bar{1}1)$ varying. This phenomenon, which has been investigated for a series of parameter combinations (t, t_0), is demonstrated for the specimen thickness $t = 1.125\xi_g$ and the depth of the inclusion $t_0 = 0.125\xi_g$ (see Fig. 1 to 3). Compared to the diversity of the contrast features in Fig. 1 to 3 a variation of the deviation parameter w around the exact Bragg orientation ($w = 0$) has a relatively small effect on the images, especially for $-0.5 \leqq w \leqq 0.5$ (dynamical excitation). The characteristics of the diffraction contrast patterns, e.g. the sign of the black–white vector, do not change. Furthermore, the intensity distribution in the defect centre is almost unmodified. However, in the BF as well as in the DF patterns the shape and extension of the contrast lobes depend on the specimen tilt.

For larger deviations $|w| \geqq 1$ the BW vector changes its sign in BF ($w = -1$) or DF ($1.0 \leqq w \leqq 2.0$) and modifications occur, particularly of the fine details, in the contrast pattern. Maintaining the two-beam case, the variation of the tilt from kinematical excitation ($w \geqq 1$) to weak-beam conditions ($w \approx 5$) leads to stronger contrast modifications because rapidly varying displacements near the defect centre increasingly determine the images. The BF contrast fades and the DF pattern dominates the LF features.

In the bottom row of Fig. 4 LF images are shown neglecting the influence of the microscope aberrations ($C_s = \Delta = 0$). Contrary to the patterns of Fig. 3, here comparable lattice fringe distortions remain in the same defect position. The visibility of

the bent as well as of terminated fringes is best for dynamical excitation with a dark residual diffraction contrast occurring. For an increasing deviation ($|w| \geqq 0.5$) from the Bragg orientation of the specimen the influence of the crystal defect on the LF contrast is reduced and vanishes. The weak-beam excitation ($w \approx 5$), however, shows strongly modified lattice fringes demonstrating the phase influence of the dilation centre approximation. The outward bending of the lattice fringes according to the chosen t_0 and t parameters is invariant for varying deviations w, the residual background due to the BF and DF patterns and fine details in shift and terminations are modified. The visibility of the defect, the BW oscillation behaviour as well as the LF features are optimum for the dynamical excitation of the two-beam situation.

7. Influence of Microscope Aberrations

In addition to the defect and specimen parameters the aberrations of the microscope imaging process influence the final image contrast. The degree of this effect is determined by the size and spatial spectrum of the defect to be imaged and by the imaging mode (diffraction contrast, lattice fringes).

The investigation of the microscope aberrations is based on the analytical and numerical methods given in [1], with the simulation of the imaging process being applied to bright-field diffraction contrast and to lattice fringe imaging in Fig. 5. As usual, the electron-optical parameters of the electron microscope are summarized in the contrast transfer function (CTF) and characterized by the most significant parameter defocus Δ. The simulations are carried out for an accelerating voltage of 100 kV, an aperture of $\alpha = 4\ \mathrm{nm}^{-1}$ in LF and with a spherical aberration coefficient of $C_s = 1.4$ mm. For three different combinations of the foil thickness t and the depth of the dilation centre t_0 ($t = 1.125\xi_g$, $t_0 = 0.125\xi_g$; $t = 1.0\xi_g$, $t_0 = 0.5\xi_g$ and $t = 11.25\xi_g$, $t_0 = 0.625\xi_g$) selected from the BF and LF images of Fig. 1 and 3 ($C_s = \Delta = 0$), here a through-focus series of $\Delta = 0$, 86 nm, and 150 nm is shown. The influence of the contrast transfer function emphasizes the residual diffraction contrast of the inclusion in the LF pattern as well as the BW lobes in BF contrast. The modifications of the BF intensity by the CTF can clearly be understood as a local periodic modulation of the diffraction contrast by the point spread function (amplification and shift) resulting in a complete change of the fine details. This is visible especially in positions having strong intensity or phase discontinuities. Analogously, the characteristic distortions of the lattice fringes remain detectable under realistic imaging conditions, but the positions, e.g. bendings and terminated fringes, are indicated by dark, blurred contrast details and are drastically modified by defocus. For $\Delta = 0$ (Gauss focus) Fresnel fringes appear, whereas for the Scherzer focus ($\Delta = 86$ nm) the relative phase rotations are minimum over a wide band of spatial frequencies. For higher underfocus ($\Delta = 150$ nm) the BW lobes increase in contrast with the fine details being more strongly modified, whereas the Fresnel fringes fade with the surrounding of the crystal defect slightly brightening.

In Fig. 6 for a dilatation centre of higher misfit ($\bar{\varepsilon} = g\varepsilon\xi_g = 20$, $R_0 = 0.05\xi_g$, $R_c = 0$) the influence of image aberrations on the BF contrast is investigated to demonstrate that the modifications can be interpreted as a local amplification and shift of the diffraction contrast itself in terms of the analytical approximations given in [1]. The ideal diffraction contrast ($C_s = \Delta = 0$) in the left column gives the standard BF image characteristics in comparison with four selected defocus values $\Delta = 0$ (Gauss focus), $\Delta = 86$ nm (Scherzer focus), and higher under- and overfocus ($\Delta = 300$ nm and $\Delta = -200$ nm, respectively). The images are calculated for an accelerating voltage

of 100 kV and $C_s = 1.4$ mm; two different foil thicknesses are selected ($t = 0.75\xi_g$ and $t = 5\xi_g$) and different depth positions of the defect ($t_0 = 0.125\xi_g$, $0.5\xi_g$, $1\xi_g$) as well as two-beam excitations ($w = 0$, 1, 5) are chosen. Due to the localized BW contrast for the very thin crystal foil circular Fresnel fringes occur in the defocused BF images. The experimental observation of these fringe structures requires a sufficient coherence of the electron wave, i.e. a weak damping envelope of the CTF. Solely for the exact dynamical excitation ($w = 0$) in thicker crystals such Fresnel fringes are obtained as fringes parallel to the phase jump at the LNC. In the weak-beam case ($w = 5$) the influences of the aberrations can be neglected, which indicates a relatively smooth intensity and phase distribution in the exit wave function. The basic features of the BW contrast remain visible in all cases irrespective of the considerable modifications of the image details for thinner crystals and the artefacts, which due to aliasing and truncation, especially, occur as manifold fringes of the image borders (see e.g. [2, 25]). The contrast details for $t = 0.75\xi_g$, however, change their direction and position proportionally to the variation of the defocus Δ, with the fine contrast being equivalent to the ideal BF image for $\Delta \geqq 0$ in the case of $w = 0$ and for $\Delta \leqq 0$ for $w = 1$ (compare the smaller black–black lobes within the extended BW contrast).

8. Influence of Polynomial Defect Eigenstrains

Fig. 7 shows calculated BF, DF, and LF patterns of a spherical inclusion according to (10) for different radii $R_c = 0.5R_0$, $0.7R_0$, $0.9R_0$, and $1R_0$ of the displacements with polynomial eigenstrains. The parameters are $a = 0$, $b_0 = 1$, i.e. they are uniform but inhomogeneous displacements within the inclusion. The simulated images correspond to $t_0 = 0.125\xi_g$, $t = 1.125\xi_g$ of Fig. 1 to 3, respectively, of the pure dilation centre; for $R_c \leqq 0.5R_0$ the contrast difference can be neglected.

For increasing R_c values the fine details in the diffraction contrast are modified, the features of the BW lobes, however, are unchanged. For the higher R_c values the contrast fades in the LF images. Residual diffraction contrast is attained only in the surrounding of the projection of the sphere boundaries into the image. This clearly demonstrates that the influence of the special analytical form of the eigenstrains on the contrast behaviour is very weak; remarkable LF distortions due to the phase difference between BF and DF only occur in the boundary region of the defect with the gradient of the displacements not being continuous.

Similar results can be obtained for other depth positions and foil thicknesses as well as for variations of the eigenstrains. Fig. 8 is concerned with the case of $t_0 = 0.125\xi_g$ (cf. Fig. 1, 2, and 3) assuming $R_c = R_0$ and $b_{-3} = 1$, $b_{-1} = 5$, $a = 5$ (Fig. 8a) as well as $b_{-2} = 1$, $b_1 = 0.5$, $b_2 = 0.2$, $b_3 = 0.2$, $a = 1$. (Fig. 8b), which means that non-uniform eigenstrains are applied. The contrast effects of Fig. 8b are very similar to those obtained in Fig. 7, whereas in Fig. 8a at the boundary of the inclusion the BW contrast is separated by a faint circle having background intensity.

Fig. 9 shows two examples of calculated BF, DF, and LF images of a spherical inclusion considering surface relaxation in the approximation for the infinite half-space (see e.g. [5, 15]). In Fig. 9a $t = 0.07\xi_g$ and $\bar{\varepsilon} = 2$ are chosen, in Fig. 9b $t = 0.125\xi_g$ and $\bar{\varepsilon} = 5$ are used. In both cases $t = 1.125\xi_g$, $R_0 = 0.05\xi_g$, and uniform eigenstrain $R_c = 0$, $a = 0$, $b_0 = 1$ are applied. Comparing the results with similar images of Fig. 1 to 3 shows the influence of the relaxation to the image contrast to be weak.

9. Influence of Many-Beam Imaging Conditions

In electron microscopy it is usually assumed that the higher resolution of many-beam imaging conditions improves the visibility of the defect fine contrast and that more information is available about the local defect structure. In the following, many-beam

calculations for the dilation centre are carried out to demonstrate that this assumption generally is not valid. The reason for this behaviour may be found in the averaging overlay process for the phases contributing to the images in many-beam cases.

Fig. 10 shows simulated BF, DF, and three-beam LF patterns for different excitations of the $(1\bar{1}1)$ and $(1\bar{1}\bar{1})$ reflexes. In Fig. 10a the $(1\bar{1}1)$ reflex is in exact Bragg position ($w_{1\bar{1}1} = 0$), whereas weak-beam conditions are realized for the $(1\bar{1}\bar{1})$ reflex. In Fig. 10b the excitation of the two reflexes is approximately reversed and in Fig. 10c both reflexes are kinematically excited ($w = 1$). The BF and both the DF images are shown, furthermore, the three-beam LF patterns are given for Gauss and Scherzer focus conditions ($\Delta = 0$ and 86 nm, respectively). While the diffraction contrast images can be interpreted in terms of slightly deformed BW contrast in analogy to the two-beam calculations; the LF patterns show only a weak influence of the inclusion on the fringe structure.

For supplementing the image calculations of three-beam LF contrast carried out by directly integrating the equations of diffraction contrast, the multislice algorithm has been applied to the sandwich model described in Section 3. The examples of Fig. 11 have been chosen out of a series of simulations with the displacement field of the dilation centre to be compared with Fig. 1 to 3; calculations using polynomial defect eigenstrains give results similar to those of Section 8 and should be published later on. The specimen thickness here assumed ($N = 21$ slices, of thickness $\Delta z = 0.288$ nm) corresponds to approximately $t = 1.5\xi_g$ for an accelerating voltage of 100 kV and gold, which has been tested by calculating thickness profiles for perfect lattices. The defect is located at a depth $t_0 = t/2$ for Fig. 11 a to c and at $t_0 \approx t/5$ for Fig. 11 d) (defect centre within slice number 5). From top to bottom BF, DF, LF, and three-beam images (HR) are shown, including the imaging parameters $U = 100$ kV and $C_s = 1$ mm in the CTF (for Δ and x see figure caption). From the left column (a) to the right one (d) the tilt of the specimen with respect to the incident beam is varied, which is characterized by the pole $\boldsymbol{p}$ of the tilt axis relative to the symmetric incidence $\boldsymbol{e} = [110]$ assumed in Fig. 11a. In Fig. 11b the tilt is $\boldsymbol{p} = 1/4(7, \bar{7}, \bar{2}\bar{0})$, and in Fig. 11 c and d $\boldsymbol{p} = 1/2(\bar{1}, 1, \bar{1})$, i.e. the $(\bar{1}1\bar{1})$-reflex is always strongly excited.

For the defect depth position $t_0 = t/2$ the BF contrast is characterized by a bright central region, which is deformed by tilting, whereas the DF images show black–white lobes of approximately the BW vector expected and LNC perpendicular to the excited $\boldsymbol{g}$ vector. With the tilt increasing the BW lobes fade. For $t_0 \approx t/5$ (Fig. 11d) in the BF the black and white areas seem to arise, but the DF contrast is rather poor; both contrasts are strongly influenced by the radial CTF. The fringe patterns due to the interference of (000) and $(\bar{1}1\bar{1})$ strong beams reveal a residual diffraction contrast according to the DF contrast features with slightly bent fringes occurring near the defect. The three-beam images (000, $\bar{1}1\bar{1}$, and $\bar{1}11$ reflexes included) are not selective with respect to the specimen tilt and the defect depth position. In the central defect region the contrast of the distorted atom columns is improved, displaying the latter more brightly than in the perfect crystal regions.

10. Conclusions

Electron microscope contrast phenomena (defocus diffraction contrast and lattice fringe imaging) of spherical inclusions have been studied by applying the computer simulation [1] considering the specimen interaction as well as the electron-optical imaging process. Calculated patterns of the bright-field, dark-field, and lattice fringe contrasts of dilation centres are compared with respect to a certain range of parameters of the specimen thickness t and the depth position t_0 of the defect, being representative of the entire contrast oscillation behaviour. The investigations are supported

by three-beam investigations and using multi-slice image calculations (see Section 9).

The associated BF, DF, and LF images of Fig. 1 to 3, respectively, demonstrate a characteristic coincidence of the contrast features. BF and DF intensities are complementary, if the absorption can be neglected. A non-vanishing absorption causes a local variation of the background intensity in the LF pattern, which decreases with increasing depth position t_0 of the defect. The visibility of the fringes is characterized by the product of the BF and DF intensities, with the thickness oscillations of the diffraction contrast determining the general fringe structure. The depth periodicity and the fine structure of the BW contrast of both the BF and the DF amplitudes describe the visibility of lattice fringes in the surrounding of the defect projection and the central region contrast.

The three types of fringe modifications discussed in Section 5 (bending, termination, displacement) are due to the phase difference between BF and DF amplitudes, which therefore is the most significant term in the present investigation. All examples calculated show that the outward or the inward bending of fringes as well as their termination and their shift are not unequivocally determined by the defect nature, because the phase shift strongly depends, for instance, on the depth position of the defect.

Deviations from the exact Bragg orientation (see Section 6) within the range of dynamical excitation ($0 \leqq w \leqq 0.5$) show that the influence of the excitation error (specimen tilt) on the final image contrast is weak. Compared to the variation of the specimen thickness and the depth position of the defect the lattice fringe distortions are confined to fixed positions in the image for varying tilt.

The fundamental features of the calculated diffraction contrast (black–white lobes and central contrast fine details) are maintained even if the microscope aberrations are considered (see Section 7), but they are modified in details. Furthermore, depending on the defocus, Fresnel fringes may occur. Unlike the ideal diffraction contrast (aberration-free, in-focus) the lattice fringe patterns are amplified and shifted due to the local variations in the phase difference between the interfering bright-field and dark-field amplitudes. Lattice fringe distortions at the inclusions are shown to be associated with residual diffraction contrast (e.g. black or white regions), whereas for many-beam imaging conditions the phase influencing behaviour seems to be lowered (see Section 9).

The fine details of the lattice fringe contrast are sensitively influenced by through-focusing. Lattice fringe distortions are blurred by the microscope aberrations because of their spatial frequency spread, but origin and local allocation are preserved. Nevertheless, the inner structure of inclusions, i.e. the eigenstrains assumed, have only small effects on fine details in diffraction contrast and lattice fringe patterns (see Section 8), they produce phase differences in BF and DF amplitudes resulting in characteristic contrast features and LF distortions.

The present work has shown that the comparison between diffraction contrast images and the lattice fringe patterns of small crystal lattice defects allows one to analyse the phase-influencing behaviour of crystal defects. Separating the different contrast features, the comprehensive study of these phase distortions supplements the defect analysis by conventional diffraction contrast techniques.

References

[1] K. Scheerschmidt and R. Hillebrand, phys. stat. sol. (a) **91**, 465 (1985).
[2] R. Hillebrand, K. Scheerschmidt, and J. Heydenreich, Ultramicroscopy **20**, 279 (1986).

[3] M. Wilkens, Electron Microscopy 1984, Proc. 8th Europ. Congr. Electron Microscopy, Vol. I, Budapest 1984 (p. 175).
[4] M. F. Ashby and L. M. Brown, Phil. Mag. **8**, 1083, 1649 (1963).
[5] K.-P. Chik, M. Wilkens, and M. Rühle, phys. stat. sol. **23**, 113 (1967).
[6] K. G. McIntyre and L. M. Brown, J. Phys. Radium **27**, 178 (1966).
[7] M. Wilkens, in: Diffraction and Imaging Techniques in Material Science, Ed. S. Amelinckx, R. Gevers, and J. van Landuyt, North-Holland Publ. Co., 1978 (p. 223).
[8] L. J. Sykes, W. D. Cooper, and J. J. Hren, Oak Ridge National Laboratory ORNL/TM-7619 Report, 1981.
[9] W. Gruschel and M. Wilkens, phys. stat. sol. (a) **89**, 467 (1985).
[10] V. V. Aristov, V. I. Nikolaichik, and I. I. Khodos, phys. stat. sol. (a) **100**, 31 (1987).
[11] S. L. Sass, T. Mura, and J. B. Cohen, Phil. Mag. **16**, 679 (1967).
[12] H. P. Degischer, Phil. Mag. **26**, 1137 (1972).
[13] D. Lepski, phys. stat. sol. (a) **16**, K43 (1973); **23**, 543 (1974); **24**, 99 (1974); **60**, 479 (1980).
[14] D. Lepski and P. Bubck, phys. stat. sol. (a) **64**, 625 (1981); **70**, 571 (1982).
[15] W. Mader, Phil. Mag. **A55**, 59 (1987).
[16] J. D. Eshelby, Proc. Roy. Soc. **A241**, 376 (1957).
[17] T. Mura, Micromechanics of Defects in Solids, M. Nijhoff Publ., The Hague/Boston/London 1987.
[18] Z. A. Moschovidis and T. Mura, J. appl. Mech. **42**, 847 (1975).
[19] A. J. Skarnulis, Thesis, Arizona State University, 1975.
[20] R. Hillebrand, Thesis, Universität Halle, 1987.
[21] F. Haider, phys. stat. sol. (a) **111**, 71 (1989).
[22] A. Charai and G. Nihoul, Phil. Mag. **A58**, 571 (1988).
[23] N. Ajika, H. Endoh, H. Hashimoto, M. Tomita, and H. Yoshida, Phil. Mag. **A51**, 729 (1985).
[24] Y. Bouazra and F. Reynand, Phil. Mag. **A51**, 815 (1985).
[25] L. D. Marks, Ultramicroscopy **12**, 237 (1984).

(Received August 29, 1989)